Nanostructure Empowers Active Tumor Targeting in Ligand-Based Molecular Delivery

Hèctor López-Laguna, Rita Sala, Julieta M. Sánchez, Patricia Álamo, Ugutz Unzueta, Alejandro Sánchez-Chardi, Naroa Serna, Laura Sánchez-García, Eric Voltà-Durán, Ramón Mangues*, Antonio Villaverde* and Esther Vázquez*

Hèctor López-Laguna, Dr. Julieta M. Sánchez, Dr Naroa Serna, Dr Laura Sánchez-García, Eric Voltà, Prof Antonio Villaverde, Dr Esther Vázquez

Institut de Biotecnologia i de Biomedicina, Universitat Autònoma de Barcelona, Bellaterra, 08193 Barcelona, Spain

Departament de Genètica i de Microbiologia, Universitat Autònoma de Barcelona, Bellaterra, 08193 Barcelona, Spain

CIBER de Bioingeniería, Biomateriales y Nanomedicina (CIBER-BBN), C/ Monforte de Lemos 3-5, 28029 Madrid, Spain

Dr. Julieta M. Sánchez

Universidad Nacional de Córdoba, Facultad de Ciencias Exactas, Físicas y Naturales. ICTA and Departamento de Química, Cátedra de Química Biológica. Córdoba. Argentina. CONICET, Instituto de Investigaciones Biológicas y Tecnológicas (IIBYT), Córdoba, Argentina. Av. Velez Sarsfield 1611, X5016GCA Córdoba, Argentina

Rita Sala, Dr Patricia Álamo Dr Ugutz Unzueta, Prof Ramón Mangues

CIBER de Bioingeniería, Biomateriales y Nanomedicina (CIBER-BBN), C/ Monforte de Lemos 3-5, 28029 Madrid, Spain

Institut d'Investigacions Biomèdiques Sant Pau and Josep Carreras Research Institute, Hospital de la Santa Creu i Sant Pau, 08041 Barcelona, Spain

Dr Alejandro Sánchez-Chardi

Departament de Biologia Evolutiva, Ecologia i Ciències Ambientals, Facultat de Biologia, Universitat de Barcelona, Av. Diagonal 643, 08028 Barcelona, Spain

Keywords: nanoparticles, self-assembling, drug delivery systems, active targeting, protein engineering, cell ligands

Cell-selective targeting is expected to enhance effectiveness and minimize side effects of cytotoxic agents. Functionalization of drugs or drug nanoconjugates with specific cell ligands allows receptor-mediated selective cell delivery. However, it is unclear whether the incorporation of an efficient ligand into a drug vehicle is sufficient to ensure proper biodistribution upon systemic administration, and also at which extent biophysical properties of the vehicle might contribute to the accumulation in target tissues during active targeting. To approach this issue, we have compromised the structural robustness of self-assembling, protein only nanoparticles targeted to the tumoral marker CXCR4, by reducing the number of histidine residues (from 6 to 5) in a histidine-based architectonic tag. By such engineering, the structure of the resulting nanoparticles, but not of building blocks, results ~~destabilized~~weakened. Upon intravenous injection in animal models of human $CXCR4^+$ colorectal cancer, the administered material losses the ability to accumulate in tumor tissue, where is only transiently found, while it instead deposited in kidney and liver. Therefore, precise and efficient cell-targeted delivery requires not only the incorporation of a proper ligand that promotes receptor-mediated internalization, but also, unexpectedly, its maintenance of a stable multimeric nanostructure that ensures high ligand exposure and long residence time in tumor tissue

Introduction

Targeting of drugs for precision medicine is a widespread popular challenge, since proper drug biodistribution is expected to enhance effectiveness and minimize undesired side effects. [1] This is especially desirable regarding cytotoxic drugs, as those used in cancer, whose administration is associated to severe toxicities. It is assumed that functionalizing drugs or drug complexes with selective cell ligands would confer active targeting and ensure their accumulation in target cells and organs where such receptor is overexpressed. However, the biodistribution analyses of antibody drug conjugates and other similarly targeted drug constructs have repeatedly revealed that the fraction of administered agent reaching the target organ is limited to around 1 %. [2] On the other hand, physical properties of drug vehicles such as surface charge, geometry and size, among others, appear as key factors influencing the tissue accumulation pattern upon systemic administration when the delivery platform is based on passive targeting,~~,~~ [3, 4] ~~when the delivery platform is based on passive targeting,~~ for instance by exploiting the enhanced permeability and retention (EPR) effect. [5] However, the weight of ~~material~~ nanoscale properties of the material itself in determining biodistribution in presence of selective cell-ligands, that is, during active targeting, remains unsolved, despite its critical value in the design of new drug delivery systems. Combining efficient homing peptides with carrier materials in their optimal configuration might largely enhance the local accumulation in target tissues above the ~1 % threshold and thus increase precision and effectiveness in the delivery process.

To discriminate between the roles of the ligand and the architecture of the vehicle itself in the process of active tumor targeting, we have engineered the modular protein T22-GFP-H6 into related constructs and tracked selected resulting variants upon administration in animal models of human colorectal cancer. Such fusion protein is composed by T22, a potent ligand of the cell surface cytokine receptor CXCR4, [6] overexpressed in several metastatic human cancers, [7] a fully fluorescent GFP and a C-terminal polyhistidine tail. T22-GFP-H6 spontaneously self-

assembles in physiological conditions as 12 nm-nanoparticles, formed by around 10 copies of the polypeptide, organized in a toroid architecture. [8, 9] and with some extent of structural flexibility. [9] When administered intravenously in orthotropic mice models of human $CXCR4^+$ colorectal cancer the fluorescent nanoparticles accumulate in primary tumor and metastatic foci at unusually high levels, estimated to represent more than 85 % of the whole-body detected fluorescence. [6] Used as a carrier of the cytotoxic drug floxuridine (FdU), the nanoconjugate T22-GFP-H6-FdU reduces the volume of primary tumor, prevents the development of metastasis and precisely destroys already formed metastatic foci in absence of detectable systemic toxicity. [10] Similar anti-tumoral effectiveness has been observed when the nanoparticles deliver, accommodated in the building blocks by genetic fusion, pro-apoptotic factors and other antitumoral peptides. [11]

Interestingly, the self-assembling of T22-GFP-H6 and related materials is driven by the overhanging polyhistidine tails that coordinate divalent cations from the media to promote stable cross-molecular protein interactions. [12] If the structure of the nanoparticle beyond the ligand itself, is relevant for precise targeting, destabilizing the supramolecular complex by modifying the histidine tail sequence would result in a potentially altered biodistribution map of the material, even if this material still contains the active CXCR4 ligand T22. The comparison of the fluorescence maps of T22-GFP-H6 and one of its less stable variants T22-GFP-H5T, once intravenously (iv) injected in colorectal cancer models, revealed that the presence of the targeting peptide T22 in the protein, although necessary for CXCR4-mediated cell binding, [6] is not sufficient for a proper tumor targeting. On the contrary, the nanoarchitecture of the material as an oligomeric supramolecular complex has a critical and unexpected impact on the fate, dynamics and final accumulation of the material at the different organs, allowing the desired biodistribution upon administration. Therefore, nanoscale organization is an unexpected key determinant of not only passive but also active targeting.

Results

Being the H6 tail critical for nanoparticle formation, [13] this end-terminal peptide was replaced in T22-GFP-H6 by alternative histidine-rich peptides of similar length, with lower content of histidine (His) residues (Table 1). Since Hh~~h~~is residues promote the cross-molecular protein-protein interactions that sustain the architecture of the oligomers, [12] the reduction in the number of Hh~~h~~is residues was expected to generate less stable nanoparticles. Then, T22-GFP-H3A, T22-GFP-H5T and T22-GFP-H5E fusions were designed, constructed and expressed in bacteria as soluble protein versions, for comparison with the parental T22-GFP-H6. The alternative His-rich segments were selected according to previous reports indicating that His residues, intersected with hydrophobic or negatively charged residues, could be still retained in Ni^{+2}-based chromatography purification that uses His residues as binders. [14]

All proteins (the parental and the derived versions) were produced as proteolytically stable full-length forms of expected molecular masses (**Figure 1A**, **Table 1**), and the specific fluorescence emission values were of the same order of magnitude than that shown by T22-GFP-H6 (Table 1). This fact indicated that native-like conformation was reached in individual GFP-based building blocks. The purification by His-tag-based affinity chromatography was efficient in all cases, but the concentration of imidazole required to elute the proteins was different in each case (Table 1). It was~~, being~~ lower, as expected, at lower His residue content. The H5T-tagged polypeptide was eluted at an imidazole concentration that represented 86 % of that required by H6-tagged materials, indicating that the strength of His-divalent cation interactions was weakened down to this relative level compared to the H6 tag. T22-GFP-H3A and T22-GFP-H5E required even less imidazole concentration for detachment from immobilized Ni, representing 68 % and 61 % of that required for T22-GFP-H6, respectively (Table 1). This fact, and the resulting quantitative data about imidazole-mediated detachment, confirmed that the strength of His-based cross-molecular interactions can be regulated by the number of His residues in overhanging tags.

In this context, s~~S~~ince the self-assembling of His-tagged T22-carrying nanoparticles is based on the ability of His residues to interact with each other's through divalent cations from the media, the quantitative reduction in the interactivity with Ni^{+2} of the engineered proteins should be translated into nanoparticles less stable than T22-GFP-H6, if they were actually formed. When checking the self-assembling of the materials in the standard carbonate buffer, all proteins spontaneously formed nanoparticles (Figure 1B, Figure 1C, Table 1), with hydrodynamic sizes and Z-potential values similar to those shown by the parental T22-GFP-H6 (Table 1). The microscopy scrutiny of all nanoparticles revealed a toroidal architecture (Figure 1C), compatible with the previously obtained molecular model of T22-GFP-H6. [8] However, when challenging the assembled materials with ionic strength, T22-GFP-H3A and T22-GFP-H5E, those with less molecular interactivity ~~with ions~~ (Table 1), immediately disassembled into smaller materials with sizes compatibles with the dimeric form of GFP (around 7 nm, Figure 1B). This was ~~,~~ indicative of weak cross-molecular interactions between building blocks. Instead, T22-GFP-H5T tolerated well the presence of salt in the media. However, this construct showed high instability during freezing and thawing and it partially disassembled as structures smaller than 12 nm (**Figure 2 A**), of size comparable to assembling intermediates described for T22-GFP-H6. [9] Some of these structures were also observed under TEM (Figure 1C). These small forms appeared together with a minor occurrence of larger protein clusters, indicative of supramolecular instability (Figure 2A), and conformational impact linked to freezing and thawing-induced damage. [15] To further assess the differential stability between H6- and H5T-based nanoparticles, they were incubated for 24 h at 37 ºC in human sera, to better reproduce the conditions of *in vivo* administration. As observed (Figure 2A), T22-GFP-H5T (but not T22-GFP-H6) nanoparticles dissociated under these conditions, confirming again the lower stability of the H5T material. Such weaker structural robustness was not due to defects in the folding of H5T building blocks, as thermal stability analysis indicated

that both modular polypeptides were equally stable (or even T22-GFP-H5T lightly more stable than T22-GFP-H6, Figure 2B). This was in agreement with the fluorescence data from Table 1.

In the light of these observations, we decided to comparatively determine the influence of nanoparticle stability on *in vivo* biodistribution ~~of both~~by comparing T22-GFP-H6 and ~~the less stable~~ T22-GFP-H5T materials. ~~nanoparticles.~~ Importantly, the modular polypeptides themselves~~, acting as building blocks of the materials~~, were both proteolytically ~~robust~~ resistant (Figure 1), structurally stable (Figure 2 C), targeted to the ~~same~~ tumoral marker CXCR4 through T22 [6, 8, 16], and only differ in a few structural amino acids at their C-termini. ~~Additionally, the thermal stability analysis indicated that both modular polypeptides were equally stable (or even T22-GFP-H5T lightly more stable than T22-GFP-H6, Figure 2B), in agreement with the fluorescence data from Table 1.~~ Also, ~~when both proteins were incubated in human serum~~ thei~~r~~ electrophoretic motility of these proteins did not change in serum, as well as their specific fluorescence (Figure 2C). ~~Moderate increases in the emission values might be indicative of structural readjustments of the building blocks, without disturbing protein integrity and folding.~~ All these data confirmed ~~that the sequence~~ that despite the differences ~~between~~ in ~~both proteins affected~~ the stability of the nanoparticles ~~but not that of~~ the ~~monomers~~building blocks were both structurally robust and competent~~, making them suitable for comparative analysis *in vivo*~~. In addition, the interactivity between T22 and CXCR4 (Figure 2D) and the ability of the peptide to mediate receptor specific endosomal internalization of nanoparticles (Figure 2E) ~~was~~ were ~~not disturbed by the modifications in the His-rich tail~~fully confirmed in both constructs.

Con formato: Fuente: Cursiva

When both T22-GFP-H6 and T22-GFP-H5T were administered iv in mice bearing subcutaneous SP5 $CXCR4^+$ colorectal tumors, the accumulation pattern of both proteins in tumor was clearly divergent. While T22-GFP-H6 was progressively found in tumor (**Figure 3A**), with a plateau of fluorescence reached at 24 h, T22-GFP-H5T was only transiently found in tumoral tissues at 5 h post administration, followed by a fast decline (Figure 3B). This might be indicative of lake or poor cell uptake in the tissue, through which the material appears to

transiently pass by. Moreover, a background (off-target) fluorescence emission of T22-GFP-H5T was observed in liver and kidney, having an increase during the 24-48 h period post-injection, whereas T22-GFP-H6 emission during this period was declining in thesc~~is~~ organs. The much more extensive and sustained T22-GFP-H6 tumor accumulation was clearly evidenced by the quantitative ex vivo analyses of relevant organs (Figure 3B). Thus, T22-GFP-H6 reached a tumor exposure (AUC = $5.04x10^8$ emitted fluorescence intensity –FLI- units / hour) 2.7 fold higher than T22-GFP-H5T (AUC = $1.90x10^8$) (**Figure 4, Table 2**). ~~The much more extensive and sustained T22-GFP-H6 tumor accumulation was clearly evidenced by the quantitative *ex vivo* analyses of relevant organs (Figure 3B). Thus, T22-GFP-H6 reached a tumor exposure (AUC = $5.04*10^8$ FLI units x hour) 2.7 fold higher than T22-GFP-H5T (AUC = $1.90*10^8$) (Figure 4 and Suppl. Table 1).~~ Mostly, background signal was observed in other non-target organs, except for T22-GFP-5HT in the 24-48 h period, which registered increases of 64% in the kidney and 14% in the liver (Figure 3C and 4B and Table 2). Consequently, T22-GFP-H6 had an AUC ~~ratio tumor~~ratio tumor/(kidney+liver) of 2.2, while in T22-GFP-H5T this ratio was 0.8 (Figure 4C). ~~-~~Since the divergence in the biodistribution maps of the two tested related proteins is irrespective of the common N-terminal ligand (T22, binding CXCR4) but dependent on the amino acid sequence of the C-terminal architectonic peptide, we ~~can~~ conclude that a multimeric organization of the modular proteins offers an appropriate nanoscale presentation of the ligand, with a geometry supporting its targeting function in the body.

Con formato: Superíndice

Con formato: Fuente: Negrita

Con formato: Sin Resaltar

Discussion

Two N-terminal homologous GFP modular proteins, namely T22-GFP-H6 and T22-GFP-H5T (Table 1), targeted to CXCR4 tumors, showed a very dissimilar biodistribution upon iv administration in mice models of human, $CXCR4^{+}$ colorectal cancer (Figure 3). Both protein versions are proteolytically stable upon bacterial production (Figure 1) and upon incubation in human serum (Figure 2 C), showing no loss, in any case, of relevant protein fragments that might abort the cell binding process. Both polypeptides are also highly fluorescent (Table 1), show robust structural stability (Figure 2 B) and spontaneously assemble as regular nanoparticles of comparable size and physicochemical properties (Figure 1C, Table 1) that equally penetrate $CXCR4^{+}$ cells in culture (Figure 2 D). However, the minor sequence differences at the His-rich C-terminal peptide (Table 1), responsible for cross-molecular interactions and divalent cation-mediated nanoparticle formation [12] resulted weakened in T22-GFP-H5T relative to the parental T22-GFP-H6, to around 86 % (Table 1). This is because of the reduction in the number of His residues in such architectonic peptide, from 6 to 5, which minimizes the binding of the protein to divalent cations, including the Ni^{+2} of the purification columns (Table 1). Other two constructs with 5 and 3 His residues in the C-terminus, respectively, are not able to form nanoparticles in high salt buffer (Figure 1B), indicative of the inability of these agents to form stable interactions. Although in contrast, T22-GFP-H5T was stable in salt, ~~the~~ long-term storage of this material at -80ºC and 24 h incubation in human serum~~,~~ at 37ºC ~~in the assembled form,~~ indicated ~~a~~ structural instability of T22-GFP-H5T nanoparticles (Figure 2 A) that was not apparent by the mere hydrodynamic size analysis upon biological fabrication (Figure 1B).

Such less stable T22-GFP-H5T nanoparticles reached the target tumor tissue at 5 h post iv administration (Figure 3). However, they failed to accumulate in the tumor (being undetectable at 24 h), while displaying a much lower tumor exposure than the parental H6-tagged protein (Figure 4). Moreover, the amounts of this protein were progressively fading in tumor tissue,

while an increased in its fluorescence signal was ~~found~~observed, at later times and at important levels, in non-tumor organs such as liver and kidney. Therefore, T22-GFP-H5T had a lower accumulation in tumor than in non-tumor tissues (AUC ratio = 0.8). This was in sharp contrast with T22-GFP-H6, for which most of the injected dose accumulated in tumor rather than in non-tumor tissues (AUC ratio = 2.2) (Figure 4, Table 2). Thus, despite T22-GFP-H6 started their tumor uptake at later times, it reached a total tumor exposure 2.7 fold higher than this achieved for T22-GFP-H5T, and also maintained a high fluorescence exposure in tumor tissue beyond 48 h. In addition to this, the injected equal dose and highly similar fluorescence emission of the two compared proteins lead to much higher tumor exposure for T22-GFP-H6 than in non-tumor tissues, while the opposite happened for T22-GFP-H5T, suggesting a more intense and faster clearance from the body of T22-GFP-H5T, since its total (tumor + non-tumor) fluorescence emission showed a 43 % reduction as compared to total T22-GFP-H6 FLI emission (Figure 4). In this regard, the higher accumulation in kidney and liver at longer times (48 h) for T22-GFP-H5T, together with its lower nanostructure stability as determined *in vitro* (Figure 2A), strongly suggests the possible occurrence of a much higher renal excretion and/or hepatic metabolism than T22-GFP-H6. The tumor accumulation pattern followed by T22-GFP-H6 was in agreement with previous experiments in related mice models. [8] This was indicative of the robustness of the material regarding biodistribution to tumor ~~tissue~~, leading to high exposure in that tissue by achieving a high uptake peak and a long residence time, while displaying low uptake in ~~non-tumor~~off-target tissues. [6, 8, 17, 18] In fact, the present data also suggested a lack of intracellular penetration of T22-GFP-H5T in tumor. When stable nanoparticles that effectively internalize in target CXCR4$^+$ tumors cells are administered, [6] a residence time of around 48 hours in tumor is consitently observed. During this time period, the nanocarrier is problably degraded within uptaking cells. [19] A 48 h residence time or longer, occurs also in therapeutic protein-only nanoparticles targeting CXCR4+ cancer cells. [20] The shorter tumor residence time of T22-GFP-H5T suggests that this protein carrier, despite

Con formato: Fuente: (Predeterminada) Times New Roman, Sin Resaltar

Con formato: Fuente: (Predeterminada) Times New Roman, Sin Resaltar

Con formato: Sin Resaltar

Con formato: Fuente: (Predeterminada) Times New Roman, Sin Resaltar

Con formato: Fuente: (Predeterminada) Times New Roman, Sin Resaltar

Con formato: Fuente: (Predeterminada) Times New Roman, Sin Resaltar

Con formato: Sin Resaltar

Con formato: Fuente: (Predeterminada) Times New Roman, Sin Resaltar

Con formato: Sin Resaltar

Con formato: Fuente: (Predeterminada) Times New Roman, Sin Resaltar

Con formato: Fuente: (Predeterminada) Times New Roman, Sin Resaltar

Con formato: Fuente: (Predeterminada) Times New Roman, Sin Resaltar

Con formato: Fuente: (Predeterminada) Times New Roman, Sin Resaltar

Con formato: Fuente: (Predeterminada) Times New Roman, Sin Resaltar

Con formato: Fuente: (Predeterminada) Times New Roman, Sin Resaltar

Con formato: Fuente: (Predeterminada) Times New Roman, Sin Resaltar

Con formato: Sin Resaltar

interacting with the CXCR4 receptor through its T22 ligand, is not effectively internalized in target cells. Consistently, an early and short residence time of GFP-H6 (lacking the T22 ligand) in tumor has been also observed. [21]

Con formato: Fuente: (Predeterminada) Times New Roman, Sin Resaltar

Con formato: Sin Resaltar

Con formato: Fuente: (Predeterminada) Times New Roman, Sin Resaltar

Con formato: Fuente: (Predeterminada) Times New Roman, Sin Resaltar

Con formato: Fuente: (Predeterminada) Times New Roman, Sin Resaltar

These data were compatible with a robust structure of T22-GFP-H6 nanoparticles compared to a progressively disassembling T22-GFP-H5T materials, provided the nanostructure is assumed as a critical component of the active targeting process. While the role of nanostructure as an element influencing passive targeting has been largely discussed and recognized, [4, 22] its potential impact on active targeting (that mediated by a cell-surface ligand) has been a rather neglected issue. Nanoscale organization of a targeted material might enhance its interaction with target cells by the multimeric binding of nanoparticles to cell surface receptor molecules ~~on the cell surface~~. [23, 24] Multivalent ligands generally show lower dissociation rates than individual versions ligands in the interaction with the receptor, [25] apart from a cooperative cell binding that promotes a more efficient early interaction and endosomal internalization. [26] Such cooperativity in both signalling and internalization of artificial constructs has been already described in different therapeutic platforms, [24, 27] what could be specially efficient in the case of symmetrically ordered materials. [28] In the case of recombinant proteins, multivalent presentation of ligands in supramolecular constructs might be more efficient than monovalent versions, [29] what has been already discused in the context of virus-like presentations of cell interactors and the consequent enhanced endosomal cell uptake. [26] In this regard, the results presented here support again the convenience of multivalent presentation, that also enhances the specificity in cell-receptor recognition. In this context, hybrid nanoparticles in which peptides R9 (an unspecific cell-penetrating peptide) and T22 (a specific CXCR4 ligand) are combined show lower CXCR4-specificity than T22 only-based nanoparticles. [13] Besides, the size increase derived from oligomerization, in the case of the modular proteins described here from ~4 nm (the hydrodynamic size of a GFP monomer) to ~12 nm, above the renal cut-off or

~6-8 nm, [18] might also increase circulation time and in consequence opportunities for a tight interaction with target tissues, promoting the desired tumor accumulation of tumor-homing materials.

Conclusion

The occurrence of an effective ligand of a tumor cell marker is necessary but not sufficient to ensure a proper tumor biodistribution of functional proteins upon systemic administration, as proved here by using a model self-assembling protein. Contrarily, a supramolecular architecture of such targeted polypeptide, in form of multimeric nanoscale materials, enables the tumor homing peptide, here modelled by the CXCR4 ligand T22, to drive the accumulation of the material in the target tumor tissue. Several factors, including the multimeric regular presentation of the ligand and the nanoscale size of the complex are probably involved in the complex process of active targeting. In active targeting, the administered material needs to overcome several biological barriers, including renal and hepatic clearance, to achieve higher exposure and residence time in tumor. The concept presented here might represent a convincing explanation of the poor biodistribution so far reached by tumor-targeted medicines, including antibody-drug conjugates. In addition to this, it is offering a potential developmental roadmap for the improvement of these drugs, of high intrinsic therapeutic potential, to reach satisfactory efficiencies in the clinical context.

((References should be superscripted and appear after punctuation.[1,2] If you have used reference management software such as EndNote to prepare your manuscript, please convert the fields to plain text by selecting all text with [ctrl]+[A], then [ctrl]+[shift]+[F9]).[3–5] Please define all acronyms except IR, UV, NMR, and DNA or similar (for a complete list of

acronyms not requiring definition, please see the list available on the journal homepage in our "Author Guidelines" section.))

Experimental Section

Genetic design, protein production and purification

The genetic design of newly ~~h~~His-derived modular proteins was based on the parental T22-GFP-H6 construction. The C-terminal H6 poly-H~~h~~is tail was exchanged for alternative his-rich human peptides under specific criteria (explained during the work). The already displayed abbreviations -H6, -H3A, -H5T and -H5E correspond to HHHHHH, HAAHAH, HTHTHTHTH and HEHEHEHEH amino acid sequences respectively. Nomenclature has been established from N to C terminal according to their modular organization. All protein sequences were designed in house as codon-optimized genes, synthetized and inserted into pET22b plasmids using NdeI and HindIII restriction enzymes and provided by Geneart (ThermoFisher). All fusion proteins were transformed by heat shock for 45 second at 42 ºC in *E. coli* Origami B (BL21, $OmpT^-$, Lon^-, TrxB, Gor^-; Novagen). Transformed cells were then grown at 37 ºC overnight in LB (Lysogeny Broth) and encoding proteins produced at 20 ºC overnight upon induction with 0.1 mM of Isopropyl-b-D-Thiogalactopyronaside (IPTG) when the OD_{550} reached 0.5-0.7. Cells were then harvested by centrifugation for 15 min (5,000g at 4 ºC) and stored at -80ºC until use. Pellets were then thawed and resuspended in Wash buffer (20 mM Tris, 500 mM NaCl, pH = 8) in presence of protease inhibitors (Complete EDTA-free; Roche Diagnostics). Cell disruption was subsequently performed by sonication (0.5-on, 0.5-off for 5 min) at 10 % of amplitude (Branson Digital Sonifier®), and the soluble fraction was separated by centrifugation for 45 min (15.000g at 4ºC) and filtered using a pore diameter of 0.45 and 0.22 m consecutively. Proteins were finally purified by Immobilized Metal Affinity Chromatography (IMAC) in an ÄKTA pure system (GE Healthcare) using HiTrap Chelating HP 5 ml columns (GE Healthcare). Protein elution was achieved by a linear gradient of Elution buffer (20 mM Tris, 500 mM NaCl, 500 mM Imidazole, pH = 8) and rinsed protein dialyzed against sodium carbonate (166 mM $NaCO_3H$, pH = 8) and sodium carbonate with salt (166 mM $NaCO_3H$, 333 mM NaCl, pH = 8) buffers.

Protein purity, integrity and concentration

Protein purity was determined by Sodium Dodecyl Sulfate Polyacrylamide Gel Electrophoresis (SDS-PAGE) and Western Blot (WB) immunoassay with an anti-GFP monoclonal antibody (Santa Cruz Biotechnology). Protein integrity was also analyzed by Matrix-Assisted Laser Desorption Ionization Time-of-Flight (MALDI-TOF) mass spectrometry and concentration determined by Bradford's assay.

Volume size distribution, Z-Potential and fluorescence emission.

Volume size distribution (VSD) and protein surface charge (Z_p) of all proteins were determined by Dynamic Light Scattering (DLS) and Z-potential measurements respectively at 633 nm and 25ºC in a Zetasizer Nano ZS (Malvern Instruments Limited) using ZEN2112 3 mm quartz batch cuvettes and DTS10170 capillary cells respectively. Measurements were performed in triplicate for error estimation and VSD peak values referred to the average mode of the populations with a rendered standard error lower than 0.01. Fluorescence emission of each GFP variant was determined at 513 nm using an excitation wavelength of 488 nm with a Varian Cary Eclipse Fluorescence Spectrophotometer (Agilent Technologies). For that, all the proteins were equally diluted in the corresponding sodium carbonate buffer w/o salt until 1 mg/ml in a final volume of 100 µl.

Ultrastructural morphometry

The nanoscale morphometry (size and shape) of self-assembled nanoparticles was determined at nearly native state, both by deposition on silicon wafers with field emission scanning electron microscopy (FESEM) and by negative staining with transmission electron microscopy (TEM). Drops of 3 µl of T22-GFP-H6, T22-GFP-H3A, T22-GFP-H5T and T22-GFP-H5E samples diluted at 0.4 mg/mL in sodium carbonate buffer were directly deposited on silicon wafers (Ted

Pella Inc., Reading) for 30 seconds, excess of liquid was blotted with Whatman filter paper number 1 (GE Healthcare), air dried for few min, and immediately observed without coating with a FESEM Zeiss Merlin (Zeiss) operating at 0.8 kV and equipped with a high resolution in-lens secondary electron detector. Drops of 3 µl of the same four samples were directly deposited on 200 mesh carbon-coated copper grids (Electron Microscopy Sciences, Hatfield) for 30 sec, excess blotted with Whatman filter paper, contrasted with 3 µl of 1 % uranyl acetate (Polysciences Inc.) for 1 min, blotted again and observed in a TEM Jeol 1400 (Jeol Ltd.) operating at 80 kV and equipped with a Gatan Orius SC200 CCD camera (Gatan Inc.). For each sample and technique, representative images of a general field and a nanoparticle detail were captured at high magnifications (from 100,000x to 600,000x).

Determination of GFP chromophore fluorescence

The GFP chromophore fluorescence dependence on the temperature of each protein was also evaluated. Fluorescence spectra were recorded in a Varian Cary Eclipse spectrofluorimeter (Agilent Technologies). A quartz cell with 10 mm path length and a thermostated holder was used. The excitation slit was~~s~~ set at 2.5 nm and emission slit~~s were set~~ at 5 nm. $_{ex}$ was ~~set at~~ 488 nm. Protein concentration was 0.2 mg/ml in the corresponding buffer.

Structural stability of protein constructs upon human serum incubation

T22-GFP-H6 and T22-GFP-H5T protein nanoparticles were incubated at 37ºC with agitation (250 rpm) at proportion 1:1 in relation to human serum (Sigma-Aldrich) for 24 and 48 h. Protein VSD was determined at 24 h by a Zetasizer Nano ZS (Malvern Instruments Limited) and protein fluorescence and motility by a Varian Cary Eclipse spectrofluorometer (Agilent Technologies) and WB immunoassay respectively. ~~T22-GFP-H6 and T22-GFP-H5T proteins were incubated at 37ºC with agitation (250 rpm) at proportion 1:1 in relation to human serum (Sigma-Aldrich)~~

~~for 48 h. Protein fluorescence emission and motility were determined by using a Fluorescence Spectrophotometer and WB blot immunoassay respectively as previously described.~~

Protein internalization

HeLa CXCR4^{+} cells (ATCC® CCL-2™) were cultured in 24-well plates (60.000 cells/well during 24 h for different time/concentration assays, in MEM Alpha 1x GlutaMAX™ medium (Gibco) supplemented with fetal bovine serum (FBS) at 37ºC in a 5 % CO_2 humidified atmosphere, until reaching a confluence of 70 %. Protein internalization was monitored at different concentrations (50 and 1000 nM) and times (1 and 24 h). After protein exposure, cells were detached and external hooked protein removed by adding Trypsin-EDTA (Gibco®) at 1 mg/mL for 15 min and 37ºC. Intracellular protein fluorescence was determined by flow cytometry using a Fluorescence Assisted Cell Sorting (FACS)-Canto system (Becton Dickinson) at 15 mW with an air-cooled argon ion laser exciting at 488 nm. Measurements were performed in duplicate. Additionally, the specific protein CXCR4-mediated internalization was proved by the addition of the receptor antagonist AMD3100 [30] that inhibits the interaction between T22 and CXCR4. This chemical compound was added at a final concentration of 500 nM (10 times protein concentration) for 1 h prior to protein incubation at 50 nM.

In vivo biodistribution assays

All *in vivo* experiments were approved by the institutional animal Ethics Committee of Hospital Sant Pau. Five-week-old female Swiss nu/nu mice weighing between 18 and 20 g (Charles River, L-Abreslle) and maintained in specific-pathogen-free (SPF) conditions, were used for the *in vivo* biodistribution studies. We used a subcutaneous colorectal cancer mouse model derived from the patient sample SP5. To generate this model, we implanted in the mouse subcutis 10 mg of SP5 tumor tissue obtained from donor animals. When tumors reached a

volume of approximately 500 mm^3 we performed biodistribution assays of T22-GFP-H6 and T22-GFP-H5T nanoparticles at three different times after nanoparticle injection, namely 5, 24 and 48 h. Mice received 100 µg single iv bolus of T22-GFP-H6 (n=2) or 100 µg single iv bolus of T22-GFP-H5T (n=2) in sodoum carbonate buffer with salt. Control animals (n=2) were iv administered with 150 µl of the same buffer.

At 5, 24 and 48 hours after the iv injection, mice were euthanized and subcutaneous tumors and normal organs, including lung and heart, kidney, liver, and bone marrow were collected. Biodistribution of GFP fluorescent nanoparticles was determined measuring ex vivo the fluorescence emitted by tumors and normal organs using the IVIS Spectrum equipment (PerkinElmer Inc, Waltham). The fluorescent signal (FLI) was first digitalized, displayed as a pseudocolor overlay, and expressed as radiant efficiency. FLI values were calculated subtracting the FLI signal from the protein-treated mice by the FLI auto-fluorescent signal of control mice.

Acknowledgements

HLL and RS have equally contributed to this study. We are indebted to Agencia Estatal de Investigación (AEI) and to Fondo Europeo de Desarrollo Regional (FEDER) (grant BIO2016-76063-R, AEI/FEDER, UE) to AV, AGAUR (2017SGR-229) to AV and 2017SGR-865 GRC to RM; CIBER-BBN (project NANOPROTHER) granted to AV and CIBER-BBN project 4NanoMets to RM; ISCIII (PI15/00272 co-founding FEDER) to EV and ISCIII (Co-founding FEDER) PIE15//00028 and PI18/00650 to RM, and to EU COST Action CA 17140. We are also indebted to the Networking Research Center on Bioengineering, Biomaterials and Nanomedicine (CIBER-BBN) that is an initiative funded by the VI National R&D&I Plan 2008–2011, Iniciativa Ingenio 2010, Consolider Program, CIBER Actions and financed by the Instituto de Salud Carlos III, with assistance from the European Regional Development Fund. Protein production has been partially performed by the ICTS "NANBIOSIS", more specifically by the Protein Production Platform of CIBER in Bioengineering, Biomaterials & Nanomedicine (CIBER-BBN)/ IBB, at the UAB sePBioEs scientific-technical service (http://www.nanbiosis.es/portfolio/u1-protein-production-platform-ppp/) and the nanoparticle size analysis by the Biomaterial Processing and Nanostructuring Unit. Biodistribution studies were performed by the ICTS "NANBIOSIS", Nantoxicology Unit (http://www.nanbiosis.es/portfolio/u18-nanotoxicology-unit/). Electron microscopy studies were performed by the Servei de Microscòpia at the UAB. AV received an ICREA ACADEMIA award. RS is supported by the ISCIII PFIS fellowship FI16/00017. LSG was supported by a predoctoral fellowship from AGAUR (2018FI_B2_00051), HLL by a predoctoral fellowship from AGAUR (2019 FI_B 00352) and UU by PERIS program from the Health Department of ~~la~~ the Generalitat de Catalunya.

Received: ((will be filled in by the editorial staff))
Revised: ((will be filled in by the editorial staff))
Published online: ((will be filled in by the editorial staff))

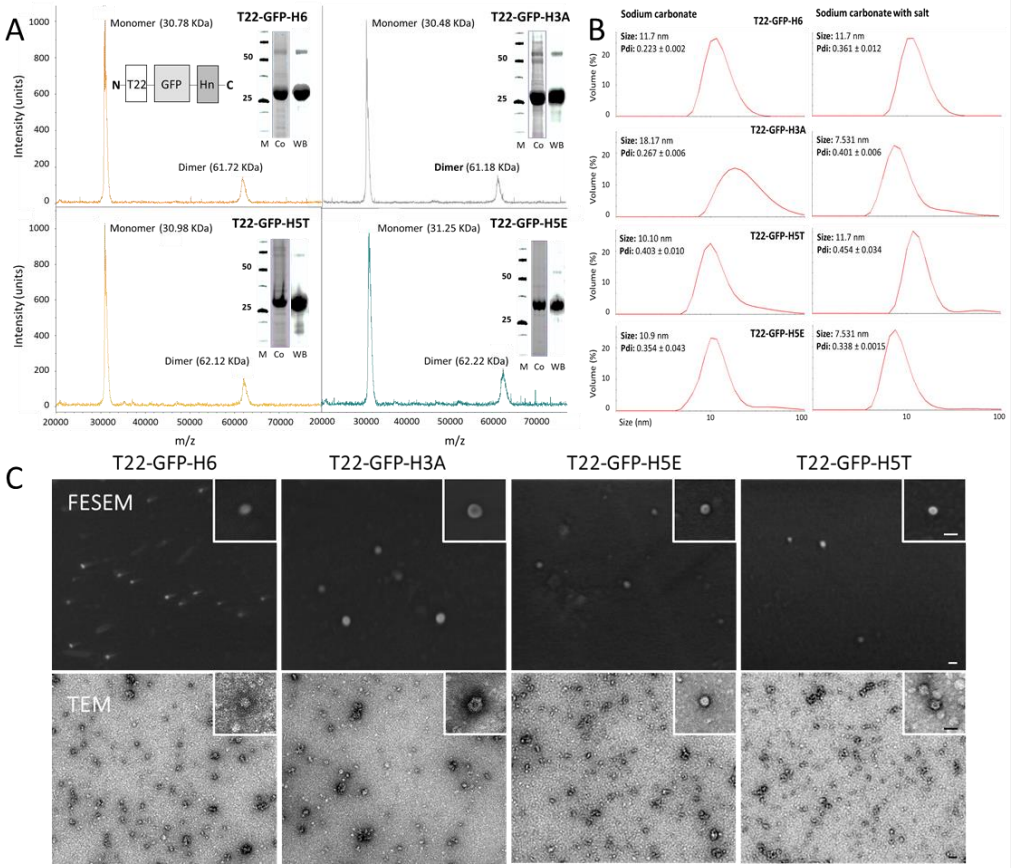

Figure 1. Physicochemical characterization of his-rich protein constructs. A. Mass spectrometry of purified samples indicating protein molecular weight of both monomeric and dimeric forms. Protein integrity was also assessed by Coomassie blue staining (Co) and anti-GFP WB respectively. Numbers indicate molecular masses (in kDa) of markers. The inset illustrates the modular architecture of the polypeptides, Hn indicating tails with variable number of His residues. B. Size distribution of his-rich protein constructions dialyzed against standard sodium carbonate buffer with or without salt. Modal peak size (nm) and PDI (Polydispersion

Index) mean± standard error values are indicated. C. FESEM and TEM imaging of his-rich protein materials in sodium carbonate buffer. Representative images showing morphometry and architecture of the nanoparticles are displayed at two different magnifications for each technique. Scale bars represent 20 nm.

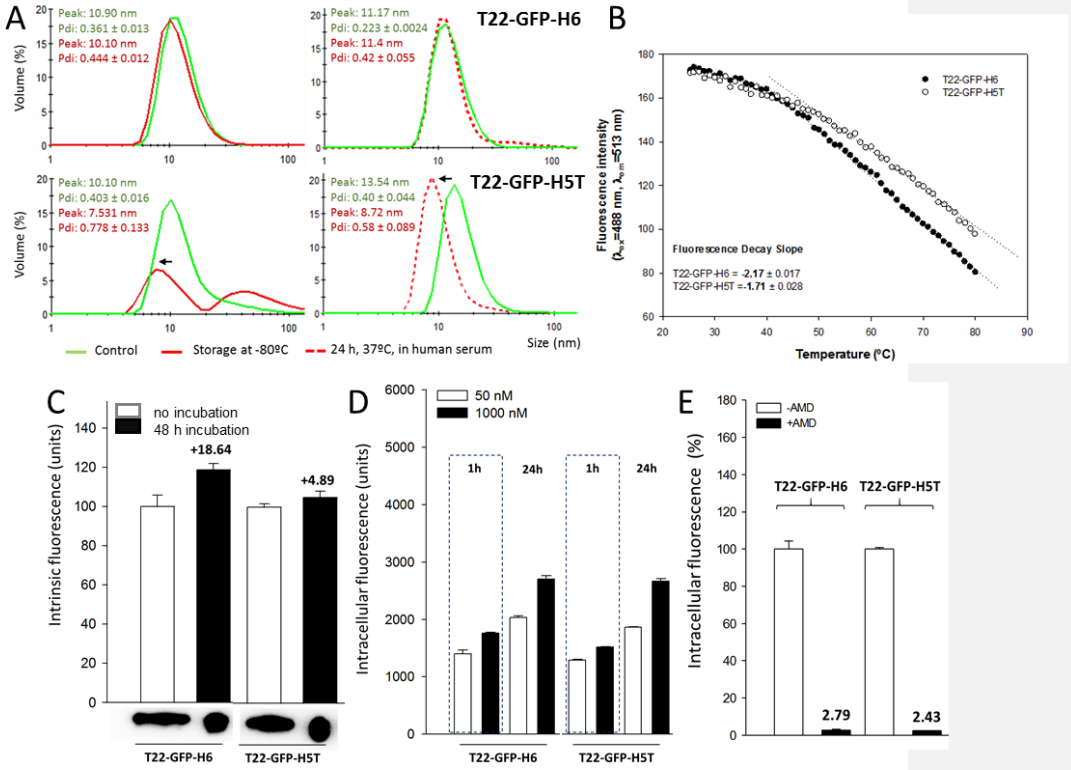

Figure 2. Structural and functional stability of protein nanoparticles. A. Size distribution of T22-GFP-H6 and T22-GFP-H5T nanoparticles upon purification and after storage a -80ºC, or upon incubation in human sera. Arrows indicate . ~~Modal~~disassembling. Modal peak size (nm) and PDI (mean ± standard error) values are indicated. B. Decrease of chromophore fluorescence intensity (at 513 nm) of T22-GFP-H6 and T22-GFP-H5T versus temperature, measured at λex = 488 nm. The slope decays from 50 to 80ºC was registered in the plot. C. Protein stability upon 48 h incubation in human serum at 37ºC. Fluorimetry (up) and western blot

immunodetection (bottom) were used to determine protein integrity. Numbers indicated on top of plot bars represent variations of fluorescence intensity in percentage relative to original samples. D. Internalization of different amounts of protein nanoparticles in cultured HeLa cells, determined at 1 and 24 h post exposure. E. Inhibition of $CXCR4^+$ cell binding mediated by the CXCR4 antagonist AMD3100.

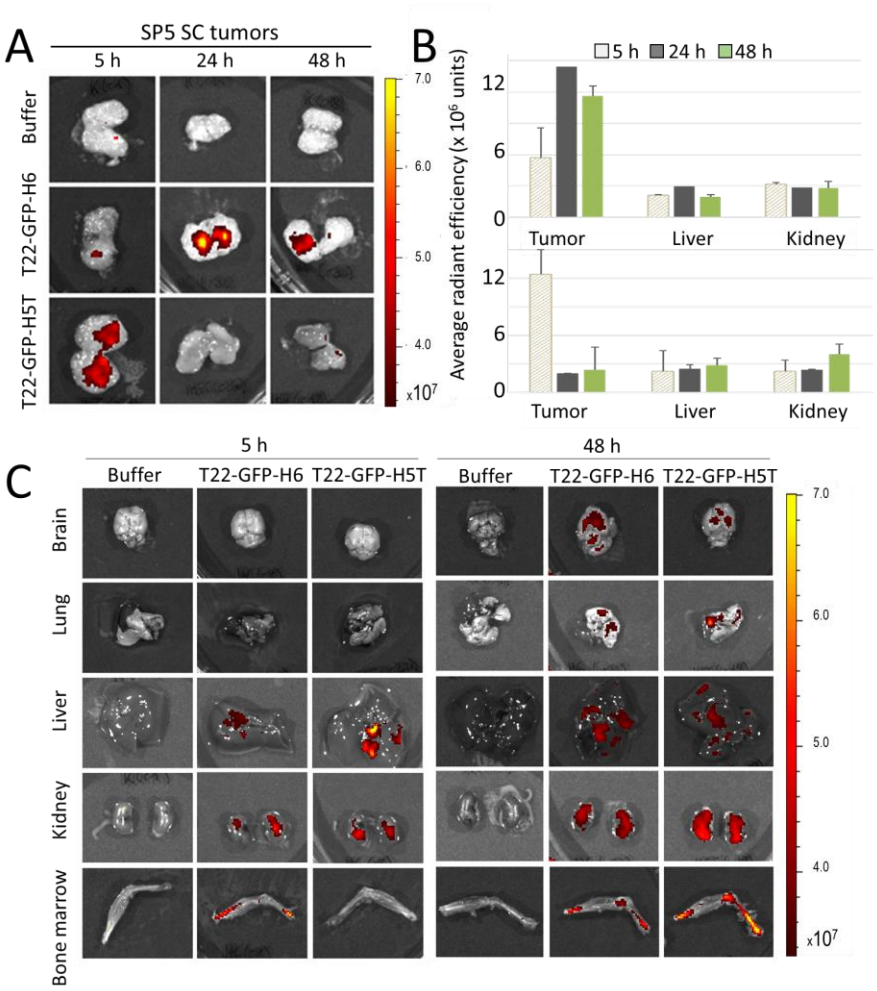

Figure 3. Tumor and non-tumoral organ biodistribution of T22-GFP-H6 and T22-GFP-H5T. A. Representative *ex vivo* tumor fluorescence images (FLI) at 5, 24, and 48 h after iv

administration of 100 µg dose of each protein nanoparticle in mice bearing subcutaneous SP5 CXCR4^{+} colorectal tumors. B. Quantitation of GFP-emitted fluorescence in tumors, liver and kidney at 5, 24, and 48 h using the IVIS spectrum system. C. Representative *ex vivo* images of nanoparticle accumulation in normal mouse organs (brain, lung, liver, kidney, and bone marrow) at 5 and 48 h.

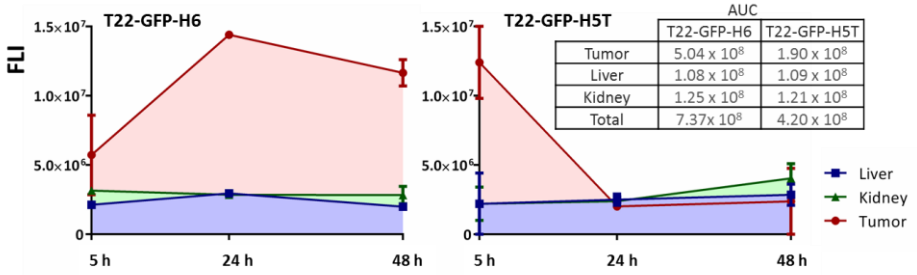

AUC

	T22-GFP-H6	T22-GFP-H5T
Tumor	5.04 x 10^8	1.90 x 10^8
Liver	1.08 x 10^8	1.09 x 10^8
Kidney	1.25 x 10^8	1.21 x 10^8
Total	7.37x 10^8	4.20 x 10^8

Figure 4. Comparison of tumor and non-tumor exposure between T22-GFP-H6 and T22-GFP-H5T in tumor bearing mice. Representation of the area under the curve (AUC) of emitted fluorescence intensity (FLI) along time (5-48 h), as a measure of exposure, registered in tumors, liver and kidney after 100 g single dose injection of T22-GFP-H6 (A) or T22-GFP-H5T (B) proteins in CXCR4+ subcutaneous SP5 patient-derived mouse models. C. Percentage of protein accumulation (as measured by the AUC = FLI x hour) in tumor, liver or kidney and total emission for both studied proteins. FLI signal from experimental mice was calculated subtracting the FLI auto-fluorescence of control buffer-treated mice. FLI, fluorescent intensity (expressed as average radiant efficiency).

Table 1. **Main properties of T22-GFP His-rich protein nanoparticles carrying modified Hhis tag sequences.**

Protein[a]	Sequence[b,c,d]	M.M. (KDa)	S.F (units/mg) ± error	H.D. (nm) / PDI ± error	Z_p(mV) ± error	I.E. (mM)[e]	I.E. (%)[f]
T22-GFP-H6	T22-*linker*-GFP-HHHHHH	30.69	9360.0 ± 198	11.7 / 0.361 ± 0.012	-17.2 ± 1.2	137.5 ± 2.5	100
T22-GFP-H3A	T22-*linker*-GFP-HAAHAH	30.49	12003.9 ± 473	18.17 / 0.267 ± 0.006	-15.1 ± 0.59	84.2 ± 3.1	61.3
T22-GFP-H5T	T22-*linker*-GFP-HTHTHTHTH	30.96	15121.8 ± 70	10.10 / 0.403 ± 0.010	-12.9 ± 0.32	119.2 ± 0.8	86.7
T22-GFP-H5E	T22-*linker*-GFP-HEHEHEHEH	31.07	10920.2 ± 79	10.9 / 0.354 ± 0.043	-16.9 ± 2.1	94.0 ± 3.2	68.4

M.M.: Molecular Mass | **S.F.**: Specific Fluorescence | **H.D.**: Hydrodynamic Diameter | **PDI**: Polydispersion Index | **Z_p**: Zeta Potential | **I.E.**: Imidazole Elution

[a] The nomenclatures 6, 3 and 5 refer to the total number of Hhis residues in the C-terminal tag and A, T and E refer to alanine, threonine and glutamic amino acids respectively.

[b] The sequence of T22 is MRRWCYRKCYKGYCYRKCR.

[c] Underlined segments correspond to the amino acids introduced in the study.

[d] The *linker* sequence is GGSSRSS.

[e] The concentration (mM) of imidazole needed to induce protein elution from Immobilized Metal Ion Affinity Chromatography.

[f] The above values (ᵉ) relative to that obtained when eluting T22-GFP-H6.

Table 2. Biodistribution kinetics of T22-GFP-H6 and T22-GFP-H5T proteins in tumor and non-tumor organs*

Organs	Groups					
	T22-GFP-H6			T22-GFP-H5T		
	5 h	24 h	48 h	5 h	24 h	48 h
Tumor	57.2 ± 28.7	144.3	116.5 ± 9.2	124.1 ± 26.2	20.1 ± 0.4	23.7 ± 23.7
Brain	26.5 ± 1.7	16.1	28.0 ± 1.7	21.8 ± 7.7	26.8 ± 5.6	23.9 ± 4.3
Lung & heart	5.6 ± 2.1	ND	10.9 ± 1.7	6.0 ± 0.9	5.0 ± 0.6	11.4 ± 1.5
Liver	21.2 ± 0.3	29.6	19.9 ± 2.0	22.1 ± 22.1	25.0 ± 4.1	28.6 ± 7.6
Kidney	31.6 ± 1.6	28.6	28.3 ± 6.3	22.1 ± 12.0	23.9 ± 0.7	40.4 ± 10.5
Bone marrow	10.9 ± 8.1	21.8	13.4 ± 0.9	2.5 ± 2.5	9.7 ± 6.7	17.4 ± 1.2

* Measures of *ex vivo* fluorescence emission by subcutaneous CXCR4+ SP5 patient-derived tumors and normal mouse organs, as measured by FLI (Protein-buffer Radiant Efficiency / 10^5) at the indicated time after iv injection of the material, using the IVIS Spectrum equipment.

Table of contents

Tumor-homing peptides are not sufficient to mediate tumor accumulation of protein materials, as demonstrated here by a set of CXCR4-targeted modular proteins that form oligomeric nanoparticles. Destabilizing the nanoscale structure by subtle protein engineering abolishes the tumor-targeting abilities of the protein, that accumulate in off-target organs instead of tumor tissues. Then, the nanoscale organization of proteins is an unexpected but critical determinant of proper targeting and biodistribution, even in ligand-empowered active targeting.

Keywords: nanoparticles, self-assembling, drug delivery systems, active targeting, protein engineering, cell ligands

Hèctor López-Laguna, Rita Sala, Julieta M Sánchez, Ugutz Unzueta, Alejandro Sánchez-Chardi, Naroa Serna, Laura Sánchez-García, Eric Voltà, Ramón Mangues*, Antonio Villaverde* and Esther Vázquez*

Title **Nanostructure Empowers Active Tumor Targeting in Ligand-Based Molecular Delivery**

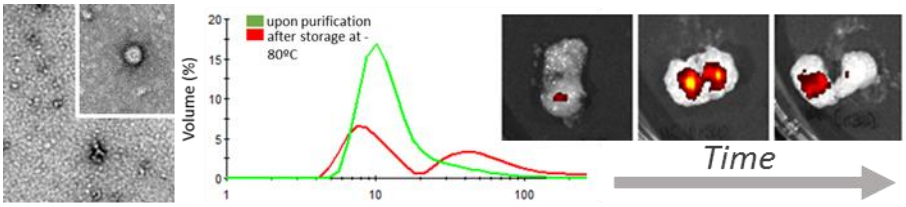

References

[1] R. V. Mangues, E; Villaverde, A, Medical Sciences 2016, 4, 6; V. J. Yao, S. D'Angelo, K. S. Butler, C. Theron, T. L. Smith, S. Marchio, J. G. Gelovani, R. L. Sidman, A. S. Dobroff, C. J. Brinker, A. R. Bradbury, W. Arap, R. Pasqualini, Journal of controlled release : official journal of the Controlled Release Society 2016, 240, 267; T. Lammers, F. Kiessling, M. Ashford, W. Hennink, D. Crommelin, G. Storm, Nature reviews. Materials 2016, 1; M. S. Lee, E. C. Dees, A. Z. Wang, Oncology 2017, 31, 198; A. David, Advanced drug delivery reviews 2017, 119, 120; K. Ozturk-Atar, H. Eroglu, S. Calis, Journal of drug targeting 2018, 26, 633.
[2] R. Duncan, R. Gaspar, Molecular pharmaceutics 2011, 8, 2101; A. J. T. Stefan Wilhelm, Qin Dai, Seiichi Ohta, Julie Audet, Harold F. Dvorak & Warren C. W. Chan, Nature Reviews Materials 2016, 1.
[3] N. Bertrand, J. C. Leroux, Journal of controlled release : official journal of the Controlled Release Society 2012, 161, 152; S. D. Li, L. Huang, Molecular pharmaceutics 2008, 5, 496.
[4] B. Mukherjee, Current pharmaceutical biotechnology 2013, 14, 1221.
[5] V. Torchilin, Advanced drug delivery reviews 2011, 63, 131; J. Reineke, Journal of controlled release : official journal of the Controlled Release Society 2018, 273, 180.
[6] U. Unzueta, M. V. Cespedes, N. Ferrer-Miralles, I. Casanova, J. Cedano, J. L. Corchero, J. Domingo-Espin, A. Villaverde, R. Mangues, E. Vazquez, International journal of nanomedicine 2012, 7, 4533.
[7] F. Balkwill, Seminars in cancer biology 2004, 14, 171; J. Kim, H. Takeuchi, S. T. Lam, R. R. Turner, H. J. Wang, C. Kuo, L. Foshag, A. J. Bilchik, D. S. Hoon, J Clin Oncol 2005, 23, 2744; J. Kim, T. Mori, S. L. Chen, F. F. Amersi, S. R. Martinez, C. Kuo, R. R. Turner, X. Ye, A. J. Bilchik, D. L. Morton, D. S. Hoon, Annals of surgery 2006, 244, 113.
[8] F. Rueda, M. V. Cespedes, O. Conchillo-Sole, A. Sanchez-Chardi, J. Seras-Franzoso, R. Cubarsi, A. Gallardo, M. Pesarrodona, N. Ferrer-Miralles, X. Daura, E. Vazquez, E. Garcia-Fruitos, R. Mangues, U. Unzueta, A. Villaverde, Advanced materials 2015, 27, 7816.
[9] M. Pesarrodona, E. Crosas, R. Cubarsi, A. Sanchez-Chardi, P. Saccardo, U. Unzueta, F. Rueda, L. Sanchez-Garcia, N. Serna, R. Mangues, N. Ferrer-Miralles, E. Vazquez, A. Villaverde, Nanoscale 2017, 9, 6427.
[10] M. V. Cespedes, U. Unzueta, A. Avino, A. Gallardo, P. Alamo, R. Sala, A. Sanchez-Chardi, I. Casanova, M. A. Mangues, A. Lopez-Pousa, R. Eritja, A. Villaverde, E. Vazquez, R. Mangues, EMBO molecular medicine 2018.
[11] N. C. Serna, M; Sánchez-García, L; Unzueta, U; Sala, R; Sánchez-Chardi, A; Cortés, F; Ferrer-Miralles, N; Mangues, R; Vázquez, E; Villaverde, A, Advanced Functional Materials 2017, 27, 1700919.
[12] H. Lopez-Laguna, U. Unzueta, O. Conchillo-Sole, A. Sanchez-Chardi, M. Pesarrodona, O. Cano-Garrido, E. Volta, L. Sanchez-Garcia, N. Serna, P. Saccardo, R. Mangues, A. Villaverde, E. Vazquez, Acta biomaterialia 2018.
[13] U. Unzueta, N. Serna, L. Sanchez-Garcia, M. Roldan, A. Sanchez-Chardi, R. Mangues, A. Villaverde, E. Vazquez, Nanotechnology 2017, 28, 505102.
[14] S. Knecht, D. Ricklin, A. N. Eberle, B. Ernst, Journal of molecular recognition : JMR 2009, 22, 270; V. Tolmachev, C. Hofstrom, J. Malmberg, S. Ahlgren, S. J. Hosseinimehr, M. Sandstrom, L. Abrahmsen, A. Orlova, T. Graslund, Bioconjugate chemistry 2010, 21, 2013.
[15] K. A. Pikal-Cleland, N. Rodriguez-Hornedo, G. L. Amidon, J. F. Carpenter, Archives of biochemistry and biophysics 2000, 384, 398.

Con formato: Español (España)

Con formato: Español (España)

[16] H. Tamamura, M. Imai, T. Ishihara, M. Masuda, H. Funakoshi, H. Oyake, T. Murakami, R. Arakaki, H. Nakashima, A. Otaka, T. Ibuka, M. Waki, A. Matsumoto, N. Yamamoto, N. Fujii, Bioorganic & medicinal chemistry 1998, 6, 1033; U. Unzueta, J. Seras-Franzoso, M. V. Cespedes, P. Saccardo, F. Cortes, F. Rueda, E. Garcia-Fruitos, N. Ferrer-Miralles, R. Mangues, E. Vazquez, A. Villaverde, Nanotechnology 2017, 28, 015102.
[17] P. Alamo, A. Gallardo, F. Di Nicolantonio, M. A. Pavon, I. Casanova, M. Trias, M. A. Mangues, A. Lopez-Pousa, A. Villaverde, E. Vazquez, A. Bardelli, M. V. Cespedes, R. Mangues, FASEB journal : official publication of the Federation of American Societies for Experimental Biology 2015, 29, 464.
[18] M. V. Cespedes, U. Unzueta, W. Tatkiewicz, A. Sanchez-Chardi, O. Conchillo-Sole, P. Alamo, Z. Xu, I. Casanova, J. L. Corchero, M. Pesarrodona, J. Cedano, X. Daura, I. Ratera, J. Veciana, N. Ferrer-Miralles, E. Vazquez, A. Villaverde, R. Mangues, ACS nano 2014, 8, 4166.
[19] A. Falgas, V. Pallares, U. Unzueta, M. V. Cespedes, I. Arroyo-Solera, M. J. Moreno, A. Gallardo, M. A. Mangues, J. Sierra, A. Villaverde, E. Vazquez, R. Mangues, I. Casanova, Haematologica 2019.
[20] L. Sanchez-Garcia, N. Serna, P. Alamo, R. Sala, M. V. Cespedes, M. Roldan, A. Sanchez-Chardi, U. Unzueta, I. Casanova, R. Mangues, E. Vazquez, A. Villaverde, Journal of controlled release : official journal of the Controlled Release Society 2018.
[21] M. V. Cespedes, U. Unzueta, P. Alamo, A. Gallardo, R. Sala, I. Casanova, M. A. Pavon, M. A. Mangues, M. Trias, A. Lopez-Pousa, A. Villaverde, E. Vazquez, R. Mangues, Nanomedicine : nanotechnology, biology, and medicine 2016, 12, 1987.
[22] E. A. Sykes, J. Chen, G. Zheng, W. C. Chan, ACS nano 2014, 8, 5696; D. Kalyane, N. Raval, R. Maheshwari, V. Tambe, K. Kalia, R. K. Tekade, Materials science & engineering. C, Materials for biological applications 2019, 98, 1252; E. Blanco, H. Shen, M. Ferrari, Nature biotechnology 2015, 33, 941; M. Alavi, M. Hamidi, Drug metabolism and personalized therapy 2019.
[23] S. Hong, P. R. Leroueil, I. J. Majoros, B. G. Orr, J. R. Baker, Jr., M. M. Banaszak Holl, Chemistry & biology 2007, 14, 107.
[24] A. Arsiwala, A. Castro, S. Frey, M. Stathos, R. S. Kane, Chemistry, an Asian journal 2019, 14, 244.
[25] C. Chittasupho, Therapeutic delivery 2012, 3, 1171.
[26] U. Unzueta, M. V. Cespedes, E. Vazquez, N. Ferrer-Miralles, R. Mangues, A. Villaverde, Trends in biotechnology 2015, 33, 253.
[27] W. Song, Z. Tang, D. Zhang, M. Li, J. Gu, X. Chen, Chemical science 2016, 7, 728; J. Reichenwallner, A. Thomas, T. Steinbach, J. Eisermann, C. E. H. Schmelzer, F. Wurm, D. Hinderberger, Biomacromolecules 2019, 20, 1118; A. Bekdemir, S. Liao, F. Stellacci, Colloids and surfaces. B, Biointerfaces 2019, 174, 367; J. F. Stefanick, D. T. Omstead, T. Kiziltepe, B. Bilgicer, Nanoscale 2019.
[28] D. S. Goodsell, A. J. Olson, Annual review of biophysics and biomolecular structure 2000, 29, 105.
[29] I. Cabrera, E. Elizondo, O. Esteban, J. L. Corchero, M. Melgarejo, D. Pulido, A. Cordoba, E. Moreno, U. Unzueta, E. Vazquez, I. Abasolo, S. Schwartz, Jr., A. Villaverde, F. Albericio, M. Royo, M. F. Garcia-Parajo, N. Ventosa, J. Veciana, Nano letters 2013, 13, 3766; Z. U. Xu, U; Roldán, M; Mangues, R; Sánchez-Chardi, A; Ferrer-Miralles, N; Villaverde, A; Vázquez, E, Materials Letters 2015, 154, 140.
[30] A. Kawaguchi, Y. Orba, T. Kimura, H. Iha, M. Ogata, T. Tsuji, A. Ainai, T. Sata, T. Okamoto, W. W. Hall, H. Sawa, H. Hasegawa, Blood 2009, 114, 2961; J. S. Song, C. M. Kang, H. H. Kang, H. K. Yoon, Y. K. Kim, K. H. Kim, H. S. Moon, S. H. Park, Experimental & molecular medicine 2010, 42, 465.

Con formato: Español (España)

Con formato: Español (España)

Con formato: Español (España)